JGR Earth Surface

RESEARCH ARTICLE
10.1029/2024JF007737

Calving Dynamics and the Potential Impact of Mélange Buttressing at the Western Calving Front of Thwaites Glacier, West Antarctica

Anna Crawford[1,2], Jan Åström[3], Douglas I. Benn[4], Adrian Luckman[5], Rupert Gladstone[6], Thomas Zwinger[3], Fredrik Robertsén[3], and Suzanne Bevan[5]

[1]University of Stirling, Stirling, UK, [2]University of Edinburgh, Edinburgh, UK, [3]CSC-IT Center for Science, Espoo, Finland, [4]University of St Andrews, St Andrews, UK, [5]Swansea University, Swansea, UK, [6]University of Lapland, Rovaniemi, Finland

Abstract The western region of the wide Thwaites Glacier terminus is characterized by a near-vertical calving front. The grounding line at this western calving front (WCF) rests on a relatively high ridge, behind which exists a reverse-sloping bed; retreat of the grounding line into this over-deepening basin could therefore expose deep calving faces that may be subject to ice-cliff failure. Here, we use the 3D Helsinki Discrete Element Model to identify the factors that control the calving dynamics in this location. We then focus on the ability of mélange to influence these dynamics given the wide embayment in which Thwaites Glacier terminates. We find that calving along the WCF is currently influenced by ice flow across the grounding line and consequent longitudinal tensile stress and rift formation. Calving is slowed in simulations that are initiated with a highly constricted mélange, with a thicker mélange suppressing calving entirely. We liken the constrained simulations to a scenario in which mélange piles behind a large grounded iceberg. In a future which may see calving become a more dominant control on the retreat of Thwaites Glacier, this type of blockage will be necessary for robust force chains to develop and transmit resistive forces to the terminus. The ability of the mélange to hinder calving at this location will be determined by the presence and rigidity of binding land-fast sea ice and iceberg keel depths. Therefore, it is necessary to represent calving, mélange and sea ice in a single framework to predict the fate of Thwaites Glacier.

Plain Language Summary Thwaites Glacier, a major outlet glacier of the West Antarctic Ice Sheet, may be vulnerable to rapid retreat. The terminus of Thwaites Glacier is over 100 km wide; in this paper, we focus on the western terminus region, which meets the Amundsen Sea at a near-vertical ice face. We use a 3D glacier model that simulates ice fracture to identify the factors controlling iceberg calving. We also run simulations to explore the potential for mélange, a conglomerate of variably sized ice pieces in front of a glacier, to impact calving dynamics at this location. Our simulations show that iceberg calving currently occurs through the growth of short ice-shelf extensions and the loss of resisting forces as the ice begins to float. Our simulations also demonstrate that calving is slowed when a thick immobile mélange is present. The ability of the mélange to apply a backforce to glaciers has been previously identified as an important brake on such calving-driven retreat. In a future that may see calving become a more dominant control on the retreat of Thwaites Glacier, this type of blockage will be necessary for the transmission of resistive forces to the terminus.

Key Points:

- Calving at Thwaites Glacier's western terminus is controlled by longitudinal tensile stresses and fracturing as basal traction is lost
- 3D modeling demonstrates that mélange, if constrained, can inhibit calving at this location
- Future sea-ice conditions and iceberg morphology will determine if mélange can compact and transmit substantial resistive forces

Supporting Information:

Supporting Information may be found in the online version of this article.

Correspondence to:

A. Crawford,
anna.crawford@ed.ac.uk

Citation:

Crawford, A., Åström, J., Benn, D. I., Luckman, A., Gladstone, R., Zwinger, T., et al. (2024). Calving dynamics and the potential impact of mélange buttressing at the western calving front of Thwaites Glacier, West Antarctica. *Journal of Geophysical Research: Earth Surface*, *129*, e2024JF007737. https://doi.org/10.1029/2024JF007737

Received 14 MAR 2024
Accepted 3 SEP 2024

Author Contributions:

Conceptualization: Anna Crawford
Formal analysis: Anna Crawford
Funding acquisition: Douglas I. Benn
Investigation: Anna Crawford, Jan Åström, Douglas I. Benn, Adrian Luckman, Suzanne Bevan
Methodology: Anna Crawford, Rupert Gladstone, Thomas Zwinger, Suzanne Bevan
Project administration: Douglas I. Benn
Software: Jan Åström, Rupert Gladstone, Thomas Zwinger, Fredrik Robertsén
Supervision: Douglas I. Benn
Validation: Anna Crawford
Visualization: Anna Crawford, Adrian Luckman, Suzanne Bevan

1. Introduction

Thwaites Glacier is a major outlet glacier of the West Antarctic Ice Sheet that has undergone dramatic changes over recent decades (Scambos et al., 2017). The glacier, which holds 65 cm of sea-level rise (SLR) equivalent, contributed 1.8 mm to global mean SLR between 1979 and 2017 (Morlighem et al., 2020; Rignot et al., 2019). The velocity of the Thwaites Tongue accelerated by 33% over the periods 1973–1996 and 2006–2013 (Mouginot et al., 2014). The glacier continues to lose mass, with a rate of 37 Gt a^{-1} calculated for 2017 (Rignot et al., 2019).

These observations, as well as findings of rapid retreat of the Thwaites Glacier grounding line in the past (Graham et al., 2022) and vulnerability to accelerated retreat in the future (Bassis et al., 2021), have focused attention on this location and other outlet glaciers of the Amundsen Sea Embayment (ASE). The vulnerability of Thwaites Glacier to rapid retreat stems from the over-deepening basin that underlies the glacier (Morlighem et al., 2020). Though the factors contributing to grounding-line migration are numerous, complex and individual to a

Writing – original draft: Anna Crawford, Douglas I. Benn
Writing – review & editing: Anna Crawford, Jan Åström, Douglas I. Benn, Adrian Luckman, Thomas Zwinger, Suzanne Bevan

concerned glacier (Sergienko & Haseloff, 2023; Sergienko & Wingham, 2022), retreat over such a reverse-sloping bed could also potentially expose deep calving faces that are susceptible to calving via ice-cliff failure (Bassis et al., 2021; Crawford et al., 2021; DeConto & Pollard, 2016; Schlemm et al., 2022).

As described by Winberry et al. (2020), the Thwaites Glacier terminus is currently divided into three regions that individually flow into, from east to west, the Thwaites Eastern Ice Shelf (TEIS), the Thwaites Tongue (TT), and a wide zone of mélange. The evolution and fate of the TEIS have recently been scrutinized by Alley et al. (2021), Benn et al. (2022), and Wild et al. (2022). Miles et al. (2020) and Lhermitte et al. (2020) respectively detail the decoupling of the TEIS and TT, and the continued shear-margin migration. This study turns its attention to the dynamics associated with failure and calving at the most westerly region of the terminus, which we refer to as the *western calving front* (WCF). This part of the Thwaites Glacier terminus meets the ocean at a mostly grounded ice front that is approximately 650–750 m thick.

Christie et al. (2022) highlight the stabilizing role of sea ice on the fracture and calving of ice shelves fringing the eastern Antarctic Peninsula. Miles et al. (2020) suggest that the presence or absence of land-fast sea ice will be a key factor in the future of the TT, noting that past calving events from the TT have coincided with break-outs of landfast sea ice. We hypothesize that the characteristics of sea ice and mélange will also play an influential role in the future dynamics of the WCF. Mélange has previously been shown to influence glacier calving and ice-shelf stability in Greenland (Amundson et al., 2010; Bevan et al., 2019; Burton et al., 2018; Cassotto et al., 2015, 2021; Joughin et al., 2020; Moon et al., 2015; Peters et al., 2015; Xie et al., 2019), Svalbard (Otero et al., 2017) and Antarctica (Khazendar et al., 2009). Previous work has also reported on the critical role of mélange in restraining calving and retreat via ice-cliff failure (Bassis et al., 2021; Crawford et al., 2021; Schlemm & Levermann, 2021; Sergienko, 2022). The ability of mélange to inhibit calving is particularly relevant to the case of Thwaites Glacier; though the controlling factors are complex and require further study, retreat over the rise in the glacier bed on which the grounding line is currently situated could lead to terminus cliff heights that are vulnerable to ice-cliff failure and marine ice-cliff instability.

Our study employs the Helsinki Discrete Element Model (HiDEM) with recently enhanced computational efficiency to elucidate the processes and factors implicated in the current fracture dynamics across the WCF. We investigate the ability of mélange to influence calving at the current WCF, and our results are discussed alongside considerations for this mélange to provide sufficient backforce to future configurations of the Thwaites Glacier terminus.

2. Methods

2.1. Remote Sensing

Sentinel-1 Synthetic Aperture Radar (SAR) scenes were used to investigate and illustrate the style of calving over several years and to derive velocity and strain maps to better understand the nature of back-force applied by the mélange. The Sentinel-1 mission consists of two satellites, Sentinel-1A (2014 to present), and Sentinel-1B (2016–2021), which together provide images and allow velocity maps to be derived every 12 days before September 2016 and after December 2021, and every 6 days between those dates. The images were multi-looked (5 in range by 1 in azimuth) before being orthorectified to a 10 m grid (EPSG:3031) and presented on a logarithmic brightness scale (−20 to +3 dB). The time-series of images was then combined into an animation (Movie S1) with a consistent time-step despite the varying interval (6 or 12 days).

Sentinel-1 velocity maps were derived using feature tracking with a patch size of 416 × 128 pixels (approximately 1 km in ground range) before being orthorectified to a 100 m grid (EPSG:3031), and strain was calculated from the velocity maps in a 3 × 3 neighborhood (Luckman et al., 2015). Here, we use example velocity and strain maps to highlight features of the calving and mélange interactions.

A time-series of digital elevation models (DEMs) based on TanDEM-X data spanning 2015 to 2022 was used to map annual grounding-line locations along the WCF. The methodology for calculating the DEMs and their height above floatation followed Bevan et al. (2021). The floatation maps were combined into annual means and the boundary between floating and non-floating ice was manually digitized.

2.2. Model Experiments

In HiDEM, ice is represented as a brittle solid by an assemblage of particles with uniform diameter that are stacked using a hexagonal close-packed (HCP) lattice. The particles are connected by elastic beams that break if the cumulative strain imposed on the beam exceeds a failure threshold. The first iteration of HiDEM (HiDEM1) is detailed in Åström et al. (2013, 2014) and van Dongen et al. (2020), and was used to simulate the calving and fracture dynamics at glaciers in Greenland (van Dongen et al., 2020), Svalbard (Vallot et al., 2018) and Antarctica (Cook et al., 2018). Investigations of glacier calving and ice-cliff failure for synthetic glacier geometries were also conducted with HiDEM1 (Benn et al., 2017; Crawford et al., 2021). HiDEM2 implements the same computational structure in a new optimized code architecture. The new version was developed by J.A. Åström and F. Robertsén at the CSC-IT Center for Science (Espoo, Finland) and was recently employed to simulate the failure dynamics of the TEIS (Benn et al., 2022). HiDEM2 v0.8 is used in this study and is simply referred to as "HiDEM."

2.2.1. Domain Preparation

The 22.7 × 10 km HiDEM domain of the WCF extends 3 to 5 km upglacier of the grounding line. This domain was a subset of a full Thwaites Glacier domain that was constructed using elevations of the ice surface, ice base and bedrock included in BedMachine v2 (Morlighem, 2020; Morlighem et al., 2020). The full Thwaites Glacier domain underwent a short surface relaxation of 2.5 days in the full-Stokes finite element model Elmer/Ice (Gagliardini et al., 2013), which adjusted ice surfaces to ensure dynamic equilibrium near the grounding line. Following the surface relaxation, ice viscosity and basal resistance were optimized sequentially through an inversion workflow (Gladstone & Wang, 2022; Wang et al., 2022) in which the MEaSUREs v2 ice-surface velocity product served as the target data set (Rignot et al., 2017). This domain preparation workflow was the same as that applied by Benn et al. (2022). Figure 1 shows the extent of the domain on a series of Sentinel-1 imagery.

Linear bed friction law was applied to calculate basal friction coefficients. Basal friction in HiDEM was rescaled by a factor of 10^{-2}. This rescaling is necessary to allow glacier sliding and fracture processes (typically hours to years duration in nature) to occur during minutes-long HiDEM simulations (Benn et al., 2022; van Dongen et al., 2020). The 3D domain that extended from the ice surface to the glacier bed contained approximately 8 million particles of 20 m diameter.

2.2.2. HiDEM Experiments

All of the HiDEM simulations in this study used a slate of standard parameter settings: beam width to particle-diameter ratio (0.6), tensile breaking strain (0.0005), and the maximum bending angle with respect to three perpendicular axes (0.03 times the maximum bending angle in radians). These three parameters along with the particle diameter and ice damage density dictate the bulk strength of the simulated ice in tension and shear. The settings were calibrated against observations of fracture and calving at Sermeq Kujalleq (Jakobshavn Isbræ, Greenland) and used in simulations that replicated observed failure of the TEIS (Benn et al., 2022). Ice damage (d), or the degree of micro-fracturing within the ice, is controlled in HiDEM2 by the probability of an inter-particle beam being broken at model initialization. This "break link probability" (BLP) of glacier ice was set to 0.3 in this study (i.e., there is a 30% chance of a bond being broken at the start of a simulation). This approach, standard in HiDEM simulations, introduces a stochastic component as the same set of bonds will not be broken at the initiation of each simulation. This can impact ice strength and stiffness at the local scale between simulations. However, the bulk properties of ice strength and stiffness will vary very little across simulations when the BLP remains constant and substantially under the threshold at which the ice fully disintegrates. This boundary between a globally connected and unconnected lattice is known as the bond percolation threshold. The BLP is also used to assign different properties to multiple ice types (e.g., glacier ice, mélange, sea ice) represented within a single simulation. The fracture property of the ice remains the same regardless of ice type as the particle-width to beam-diameter ratio, tensile breaking strain and maximum bending angle remain constant across simulations. The standard settings and those used during the model experiments are included in Table 1.

The WCF model domain extended across a region of the Thwaites Glacier terminus with a high across-flow velocity gradient. Force was therefore applied to the inflow boundary to represent this variation in velocity. The force application was informed by a MEaSUREs v2 velocity transect that corresponded to the inflow boundary of the HiDEM domain. The application of a force to the inflow boundary has been necessary in past

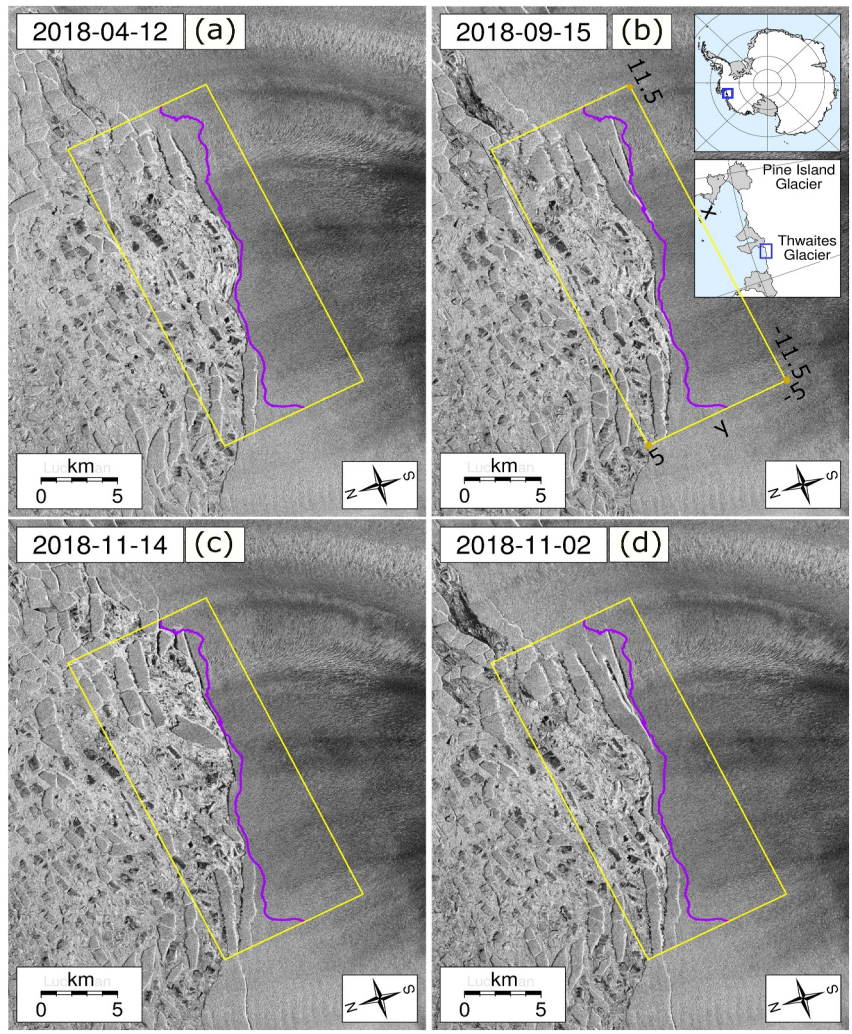

Figure 1. A calving cycle at the Thwaites Glacier western calving face (WCF) illustrated through a series of Sentinel-1 scenes (EPSG:3031). An animation with the full series of Sentinel-1 imagery between 2017 and 2024 is included in Movie S1. The spatial coverage of the HiDEM domain of the WCF is shown with a yellow box. The horizontal extents of the HiDEM simulations are noted with coordinates, in km, specific to the HiDEM domain. These correspond to the x- and y-coordinates included in Figures 2, 5, 6, 9. and 10. The location of Thwaites Glacier as part of the Antarctic Ice Sheet is noted with the blue box in the top inset of (b), with the location of the WCF noted in the bottom inset. The purple lines denote the annual grounding-line location as determined by digital elevation models derived from TanDEM-X data. These panels contain modified Copernicus Sentinel-1 Synthetic Aperture Radar data (2014–2020) processed by ESA.

HiDEM simulations (Åström & Benn, 2019; Åström et al., 2021) and the distribution of the applied forces in this study mirrors the application by Benn et al. (2022).

To assess the influence of undercutting on the calving dynamics of the WCF, we ran a simulation where any undercut is removed, that undercut being inherent in small portions of our original domain given the surface (REMA) and bed (BedMachine v2) fields. The undercut was in-filled with glacier particles, which forced a vertical ice face at the calving front. Another simulation was run with an artificial undercut initiated with a 0.16:1 basal surface slope in the eastern terminus region of the vertical ice-face domain. This domain resulted in a terminus with enhanced stress imbalances. Figure 2 provides illustrations of these domains.

The ability of the mélange to influence calving dynamics at the WCF was assessed with a series of HiDEM simulations in which mélange thickness and strength were adjusted. In our simulations, particles had a diameter of 20 m and no bonds were created between the mélange and the glacier ice. The mélange fields had uniform thicknesses of either 20 or 52 m and were subjected to buoyancy force. The mélange strength was modified by

Table 1
HiDEM Parameter Settings

Parameter	Value
Beam width: particle diameter	0.6
Tensile breaking strain	0.0005
Maximum bending angle (radians)	0.03
Young's modulus (Pa)	1×10^9
Initial damage of glacier ice ("d"; probability of an initially broken bond)	0.3
Friction scale	0.01
Particle size (m)	20
Timestep (s)	0.001
Duration of simulation (s)	1,000

increasing d, for the mélange only, from 0.4 (strong) to 0.7 (weak) to 0.88 (very weak). The latter two assignments were chosen to test the crossing of the bond percolation threshold of a bulk HCP lattice (0.88) and a 2D triangular lattice (0.65). Our rather thin (in number of particle layers) mélange fields are not percolating with $d = 0.7$ (20 m thickness) or $d = 0.88$ (20 or 52 m thickness). All simulations in which mélange was included were run with the same inflow push as applied to the earlier simulations without mélange.

A barrier across the domain that constrained the sea-ward movement of mélange particles was imposed in a subset of simulations to test the implications of a constrained versus unconstrained mélange. Mélange particles could not flow out of the domain during the simulations that applied this barrier, which we interpret as an impediment such as a large grounded iceberg. A schematic of the array of simulations that were run in our experiments is provided in Figure 2e.

The simulations were run over 1,024 cores on ARCHER2, the UK Research and Innovation supercomputer housed at the University of Edinburgh. The parameter settings used in all simulations are provided in Table 1. All simulations were run for 1,000 s. This is considered the dynamic time of the simulation and is the time scale over which the relaxation of stresses within the mélange occurs. The speed at which fracture and glacier motion occur in HiDEM simulations is directed by the friction-scale factor, and the represented glacier "sliding time" is equivalent to the duration of the simulation, in s, divided by the friction scale. The sliding time of the full

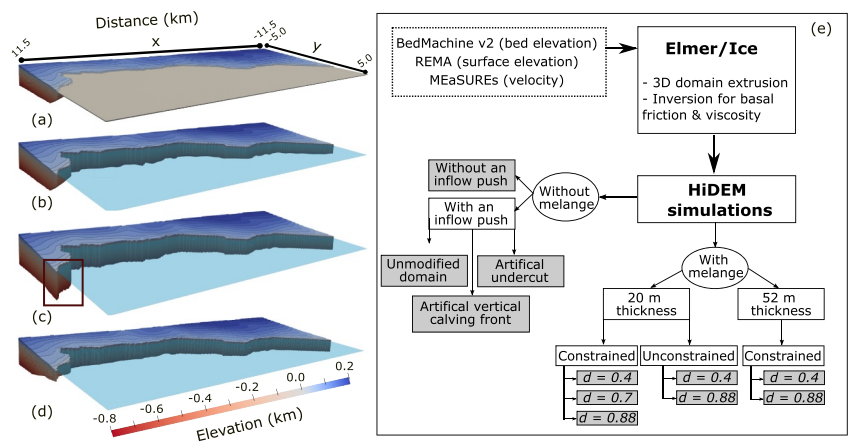

Figure 2. Illustrations of the HiDEM domains are shown in panels (a) through (d), with particles colored based on elevation relative to the waterline: (a) is the original glacier domain with a synthetic, 20 m thick mélange field extending from the calving face and the boundary coordinates of the domain noted, (b) is the original glacier domain without a mélange field, (c) is the domain with an artificial vertical calving face, and (d) is the artificial undercut domain. The transparent blue plane in panels (b) through (d) depicts the waterline. The box in panel (c) highlights one location along the calving face where the changes between the original undercut, vertical calving face, and artificial undercuts are apparent. Panel (e) is a schematic of the simulation workflow, where d = damage.

Table 2
Summary of HiDEM Simulations Run With a Synthetic Mélange

Simulation	Mélange thickness (m)	Mélange *d*	Mélange constraint
1	20	0.4	uc
2	20	0.7	uc
3	20	0.88	uc
4	20	0.4	c
5	20	0.88	c
6	52	0.4	c
7	52	0.88	c

Note. d = the probability of an initially broken bond and represents the initial strength of the mélange, uc = unconstrained, c = constrained.

simulations presented here is approximately 28 hr. Table 2 provides a summary of the various simulations conducted with a synthetic mélange.

The pressure applied by mélange to the glacier calving face, and pressure within the mélange field, was calculated following a post-processing workflow in Python that employed graph theory to discern between the glacier and mélange. The largest assemblage of connected particles was identified as the glacier, with all other particles then being assigned to the mélange. Pressure was calculated across mélange and glacier particles that were within 22.45 m, this being the particle size multiplied by a factor of 1.1225. The HiDEM particle size is scaled by this factor to obtain a closed-packed lattice with particle layers of unit width. The scaling factor is dictated by the distance $\sqrt{(6)}/3\times$ particle diameter between layers of an HCP lattice. The pressure was binned in 500 m increments to assess variation in the depth-integrated mélange force across the calving front. Pressure between bonded mélange particles was calculated to assess the spatial and temporal variation within the mélange field.

3. Results

3.1. Observations of Calving and Mélange Characteristics

Calving at the WCF follows a consistent cycle throughout the 2014–2022 study period. An animation of this calving behavior is included in Movie S1 and an example cycle is depicted in Figure 1. First, ice is advected across the grounding line, forming a temporary ice shelf. Second, as the shelf grows, rifts are formed at or close to the grounding line and grow laterally. Third, ice calves along the rifts, shifting the ice front back to the grounding line. The shelf typically attains a length of 1 to 2 km prior to calving. Calving releases tabular bergs at the eastern and western ends of the WCF. In the central part, however, many icebergs overturn either immediately upon calving or following the break-up of tabular bergs. It is clear from the pattern of calving that the position of the ice front correlates with a zone of high longitudinal strain at the grounding line, where basal resistance vanishes. The "calving rate" therefore is simply a function of the rate at which ice is delivered to the grounding line.

Icebergs released by calving at the WCF form a dense mélange that typically flows seaward as a coherent mass, suggesting bonding by sea ice (Figure 3a). Occasionally, extensive "break-out" events occur (Figures 3b–3d), during which icebergs are transported more rapidly away from the WCF, with independent trajectories of individual bergs. Throughout the study period, mélange motion appears to be unconstrained, with the exception of a persistent zone of compression and extension as mélange adjacent to the WCF passes a localized bathymetric high (Figure 4).

3.2. The Influence of Ice Flow and Undercutting on Calving Dynamics

Figure 5 illustrates the results of initial HiDEM simulations without mélange, without (Figure 5a) and with (Figure 5b) ice push at the upglacier boundary of the domain. In the absence of ice push, calving did not occur in any part of the domain. In contrast, calving did occur in the eastern portion of the domain when an inflow push was applied. The reasons for this contrast can be understood from Figure 5, which shows the cumulative maximum and minimum horizontal principal strains at approximately 28 hr of sliding time. Positive principal strains shown in green are extensional. These strain magnitudes are much greater than the observed strain (Figure 4), given that the simulations are initiated without crevasses; therefore, our simulated strains include the significant strains that appear during fracture formation, while observations mainly cover periods of gradual crevasse widening. Elevated strain in the eastern portion of the domain is markedly absent in the "no-push" HiDEM simulation, while a zone of high extensional strain along this portion of the calving face is apparent in the simulation in which an inflow boundary condition is applied. As the ice is pushed across the grounding line and basal traction is lost, enhanced strain leads to the formation of rifts behind the short ice-shelf extension. Calving of an iceberg is imminent, which corresponds closely to the calving cycle observed in the Sentinel-1 imagery.

No calving occurred in the western part of the domain in the inflow push scenario. We interpret this as the result of lower ice-push displacement in the simulation, reflecting lower observed ice velocities in this region. During the simulation, the ice front advanced only 52 m in the west, compared with 150 to 200 m in the east. This was

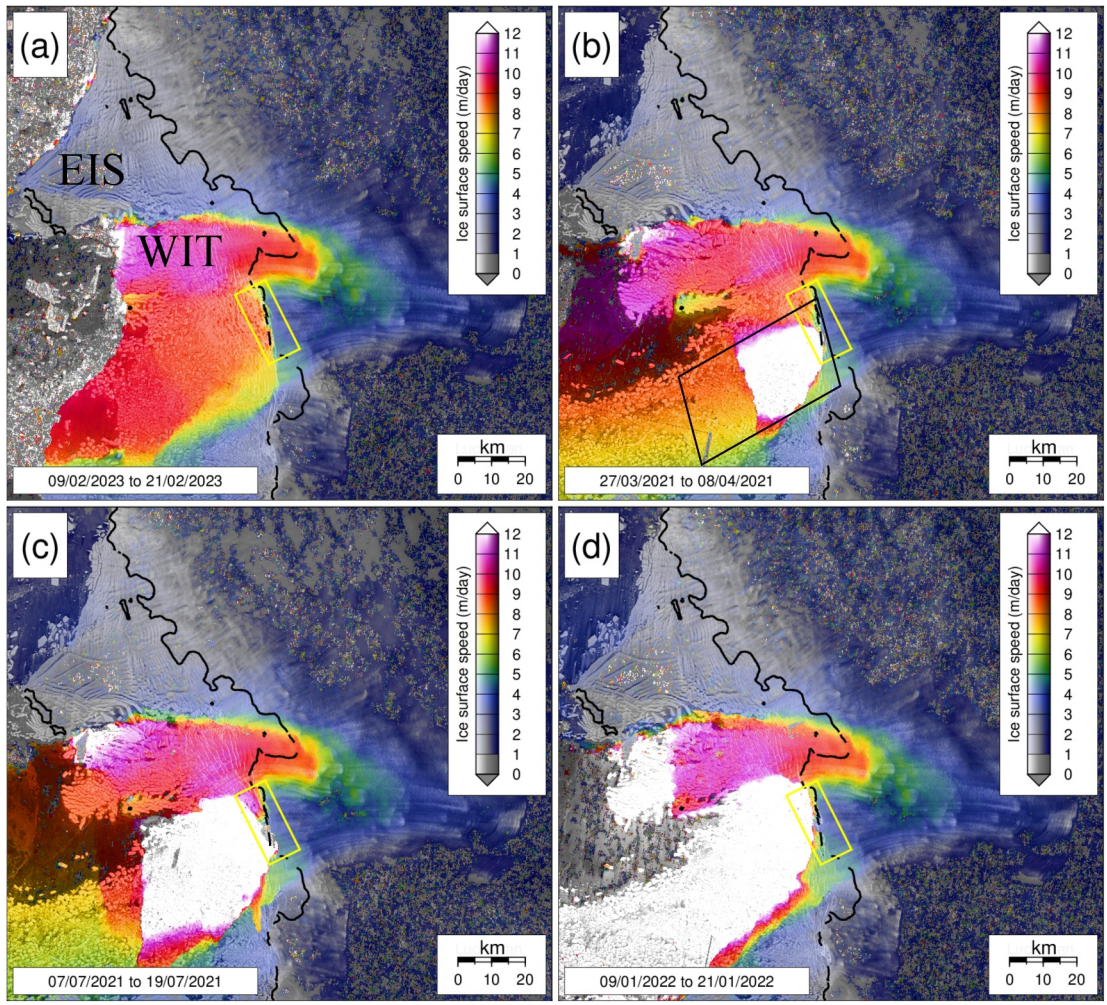

Figure 3. (a) Typical velocity field across the Thwaites Glacier terminus. (b)–(d) Example break-out events in the mélange field as seen with the loss of coherence in feature tracking. The background image in greyscale is the Copernicus Sentinel-1 (ESA) backscatter scene of the first image of the pair used to create each velocity map. The approximate location of the mélange field is marked by the black box in panel (b). The 2011 InSAR-derived grounding line (MEaSUREs; Rignot et al., 2016) is in black. The yellow box covers the HiDEM model domain. EIS = Eastern Ice Shelf. WIT = Western Ice Tongue.

apparently not enough to trigger calving. It is notable, however, that zones of extensional strain occur in the west in both "no-push" and "push" simulations, which could culminate in tabular calving events following sufficient ice advection.

Calving was almost non-existent in the western region of the domain when the undercut was replaced with a vertical calving face, though the promontory at the eastern edge of the domain still showed calving activity. Instability led to enhanced calving and clear retreat when an artificial undercut was applied (Figure S1 in Supporting Information S1). Together, these simulations demonstrate the influence of ice movement across the grounding line and undercutting on calving dynamics at this location.

3.3. The Influence of Mélange Characteristics on Calving

Simulations include a synthetic mélange, show that after 28 hr of sliding time, the greatest fracture and calving of the WCF occurs when the mélange is unconstrained (i.e., able to escape the domain) (Figures 6a and 6b). Calving and macro-fracture development occur even if the unconstrained mélange itself is strong (Figure 6b), with greater fracturing relative to the simulations with a constrained mélange (Figures 6c and 6d).

When constrained, a strong ($d = 0.4$), 20 m thick synthetic mélange slows fracture growth and no icebergs calve within 28 hr of glacier sliding time (Figure 6c). Macro-scale fractures are absent when a constrained mélange field

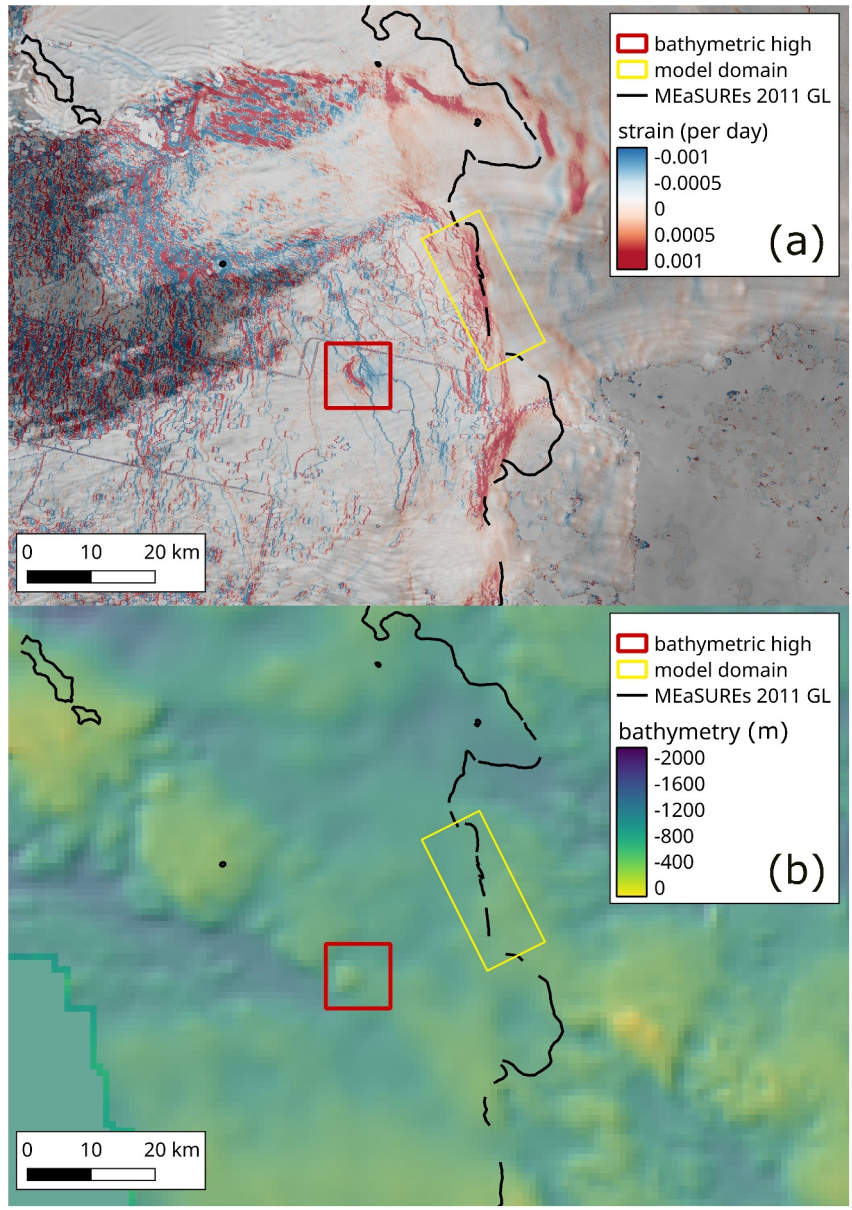

Figure 4. A zone of compression and extension (panel (a), red square) as mélange adjacent to the western calving front passes a bathymetric high (panel (b), red square). A retrograde bed slope is shown upglacier of the HiDEM model domain within the yellow box. The 2011 InSAR-derived grounding line (MEaSUREs; Rignot et al., 2016) is in black. The strain is computed from the mean Copernicus Sentinel-1 velocity derived from all 6 and 12-day image pairs during 2021 (131 individual velocity maps). The background image is the mean backscatter also for 2021. The glacier bed and bathymetry in panel (b) are from the BedMachine v2 data set (Morlighem, 2020).

of the same strength is thickened to 52 m. Pressure ridges develop within the mélange field (Figure 6d). Such pressure ridges develop as the result of the buckling within a mélange field once it is no longer able to maintain planar orientation due to elevated compression. Ridging is not observed in the constrained simulation with a thinner mélange. Instead, there is displacement of the mélange that is in close proximity to the glacier and some new mélange is added following small glacier calving events.

Simulations with a constrained but weaker ($d = 0.88$) mélange were run for simulations with 20 and 52 m mélange thicknesses (Figure S2 in Supporting Information S1). The fracturing to the far east of the domain is more advanced in both simulations with a weaker mélange compared to a stronger mélange of the same thickness. This fracturing is still very limited and pressure ridges are again observed in the simulation with a 52 m-thick mélange.

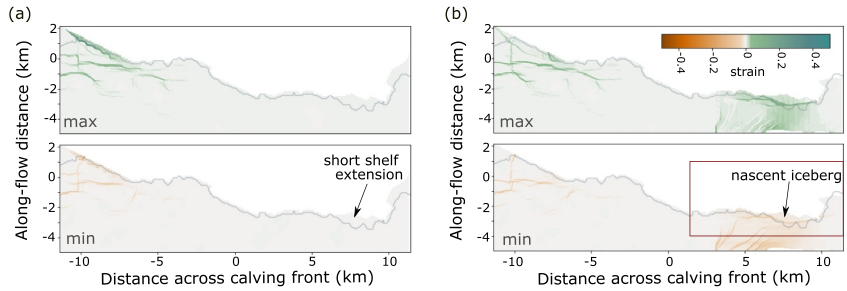

Figure 5. Influence of inflow boundary conditions on the calving dynamics of the western calving front at Thwaites Glacier at 28 hr of sliding time in the HiDEM simulations. The inter-particle strain calculated across the full duration of the simulations and averaged over elevations above the waterline is depicted with the maximum ("max") and minimum ("min") principal strain for simulations with the original domain (a) and the same domain with an inflow boundary condition applied (b). Strain increases as the glacier ice in the eastern (right-hand) portion of the domain moves past the grounding line, denoted by the thin gray line, when an inflow boundary push is applied. The mélange created through iceberg calving is not included. The box in the lower panel of (b) is the extent shown in Figure 6. Promontories exist between approximately −11 to −3 km and 9.5 to 11 km along the calving front.

3.4. Spatially and Temporally Varying Mélange Forces

The difference in the compressive force imparted along the calving face between the simulations with constrained and unconstrained mélange is illustrated in Figure 7a. At 28 hr of glacier sliding time, simulations with a constrained and thick (52 m) mélange had elevated depth-integrated force extending over greater portions of the glacier calving face in comparison to simulations with a constrained and thin (20 m) mélange or when the initial and newly calved components of the mélange were not restricted in movement (Figure 7a). The curvature of the terminus is implicated in the variation of the pressure across it, with increased pressure generally seen where the terminus extends further in the along-flow direction. There are two possible contributions to this observation: promontories are in general more prone to high pressure and/or they experience more backforce because they are in closer proximity to the source of restriction.

Figure 8 shows the probability density function of compressive force between interacting glacier and mélange particles and illustrates that, while there is a large variation in the pressure exerted on individual particles, the majority of the pressure force is applied through a small fraction of the mélange–glacier particle interactions. This is the case regardless of mélange strength or simulation run time. Interestingly, the distribution of the compressive

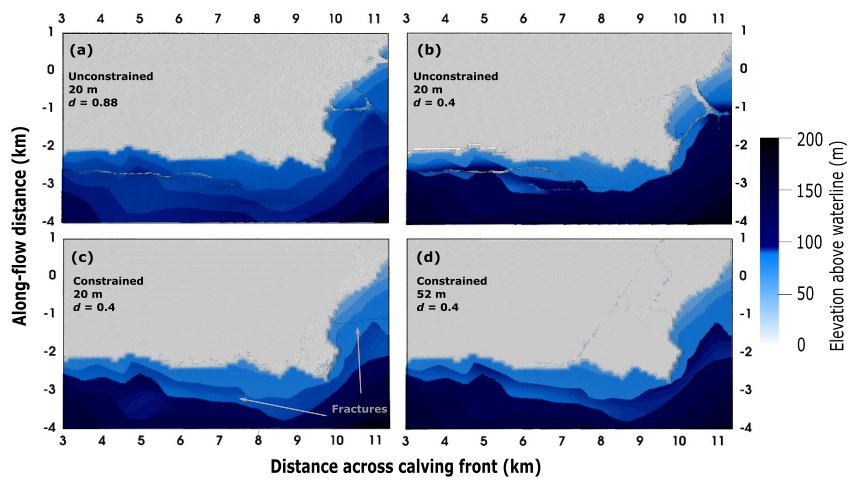

Figure 6. Calving and fracture of the eastern portion of the domain at 28 hr of glacier sliding time in HiDEM with an unconstrained (a, b) and constrained (c, d) mélange. The extent of the shown domain is noted in Figure 5. Augmented calving and fracture occurs when the mélange is unconstrained, reduced when constrained (c) and inhibited when constrained and thickened (d). The thickness of the synthetic mélange is noted (20 or 52 m) and *d* is the initial damage value assigned to the mélange.

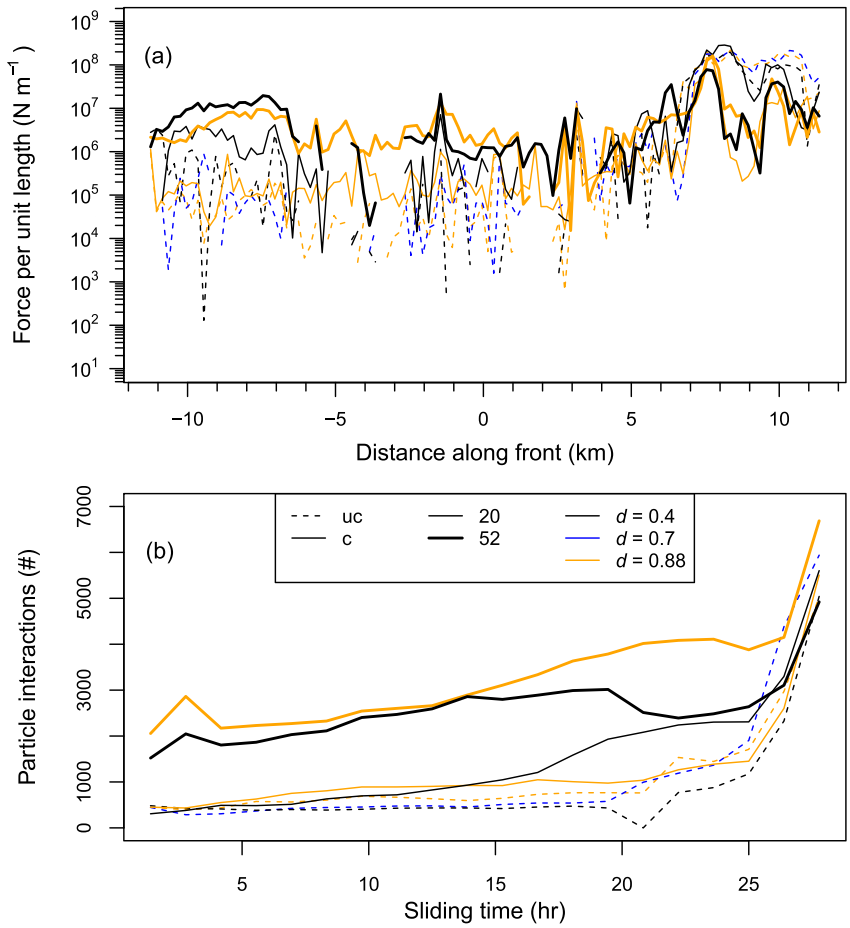

Figure 7. (a) Depth-integrated mélange force on the western calving face of Thwaites Glacier at 28 hr of glacier sliding time in the HiDEM simulations. Promontories exist between approximately −11 to −3 km and 9.5 to 11 km along the calving front. The distance along the calving front corresponds to that shown in the 3D domain in Figure 2a. (b) Number of glacier-mélange particle interactions over the duration of the HiDEM mélange simulations. The thickness of the synthetic mélange is noted as either 20 or 52 m, *d* is the initial damage value assigned to the mélange, and "uc" and "c" refer to unconstrained and constrained mélange simulations, respectively. The legend in panel (b) corresponds to both plots.

forces between in-contact glacier and mélange particles showed no clear difference across simulations initiated with varying mélange strength or thickness at the end point of the simulations (Figure 8d). Instead, variation in pressure exerted by the mélange along the WCF was more apparent earlier in the simulations. At 7 hr of sliding time, greater compressive forces were found between interacting glacier and mélange particles in the simulations with constrained strong mélange (Figure 8a). At this point in the model run time, the median pressure on the terminus in the two constrained and strong mélange simulations was 0.03 (IQR: 0.008–0.09) and 0.04 (IQR: 0.01–0.1) MPa for 20 and 52 m thicknesses, respectively. This was two to four times greater than the other simulations.

The strong, constrained mélange that characterized these simulations imparted adequate compressive force on the glacier face at the initiation of the model run to slow fracture development. In contrast, the lesser compressive force imparted early in the simulations by unconstrained or weak mélange (Figure 8a) allowed fractures to initiate and for the seaward displacement of glacier particles. The latter resulted in more glacier particles to come into contact with mélange and elevated the compressive forces between glacier and mélange particles as these simulations with unconstrained or weak mélange progressed. This is especially apparent with the depth-integrated mélange backforce at the end of the constrained, weak (d = 0.88) and thick (52 m) simulation (Figure 7a), which had an elevated number of glacier-mélange particle interactions compared to other simulations (Figure 7b). Other simulations showed an increase in the number of glacier-particle interactions after approximately 26 hr of glacier sliding time (Figure 7b). This increased the total force on the glacier calving face in all cases, but this was

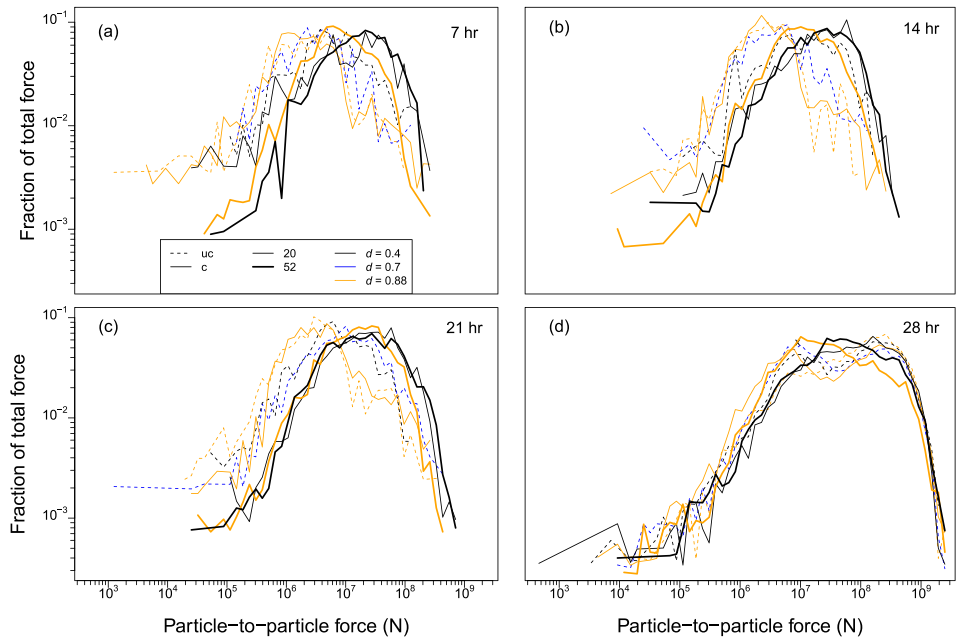

Figure 8. Fraction of total force exerted through individual mélange–glacier particle interactions over the course of simulation. The force exerted at the duration of glacier sliding time in the HiDEM simulations is plotted, with the sliding time noted in the top right of each panel. Logarithmically spaced bins were used to create the probability density function. The characteristics of the mélange field for each simulation are noted with uc = unconstrained, c = constrained, d = damage. Mélange thickness is either 20 or 52 m.

consolidated in the eastern region for the simulations with an unconstrained mélange that saw calving in that part of the domain (Figures 6 and 7a).

The total force exerted on the calving face was 78% lower for the simulations with a thinner constrained mélange when compared to the thicker constrained mélange simulations with the same damage characteristic. This is expected given the greater number of particle interactions in the simulations with the thicker mélange. The reduced force imparted on the calving face allowed more fractures to develop in the simulations with a thin constrained mélange relative to the simulations with a thicker and constrained mélange. However, the fractures remained minor compared to those that developed in simulations in which the mélange was unconstrained.

Figure 8 shows a general pattern of diminishing compressive forces as the pressure relaxed somewhat in the expanding mélange over the course of the simulations with an unconstrained mélange. However, the pressure distribution largely shifted to greater particle-to-particle pressure magnitudes with the seaward displacement of glacier particles as fracturing progressed in these simulations. Together, these processes resulted in the compressive force distributions becoming largely similar toward the end of the simulations.

In summary, the compressive forces exerted between the in-contact glacier and mélange particles relaxed to, more or less, the same distribution function by the end of the simulations (Figure 8d). While mélange stresses will relax over dynamic time scales of a few minutes, glacier sliding is, in reality, 100 times slower than represented in our simulations. The backstress on the glacier calving face will almost always stay close to the universal distribution function for per-particle backstress on the glacier shown in Figure 8d. However, Figures 8a–8c illustrates that mélange fields of varying characteristics react differently to rapid transients in glacier motion (e.g., calving or fracture development) and a strong transient mélange reaction is more able to inhibit calving.

Pressure on the calving face can also be enhanced through jamming within the mélange or as a transient response following a calving event. Through visualization of the compressive forces within the mélange in Figure 9, we see that the simulations with a constrained mélange transferred compressive stresses back to the glacier calving face with the formation of highly developed force chains stemming from the shear compression initiated by the impenetrable downstream boundary of the domain (Figures 9a–9d). This represents a situation in which the mélange builds up behind a large iceberg or sea-ice floe or is otherwise restricted in its movement. The

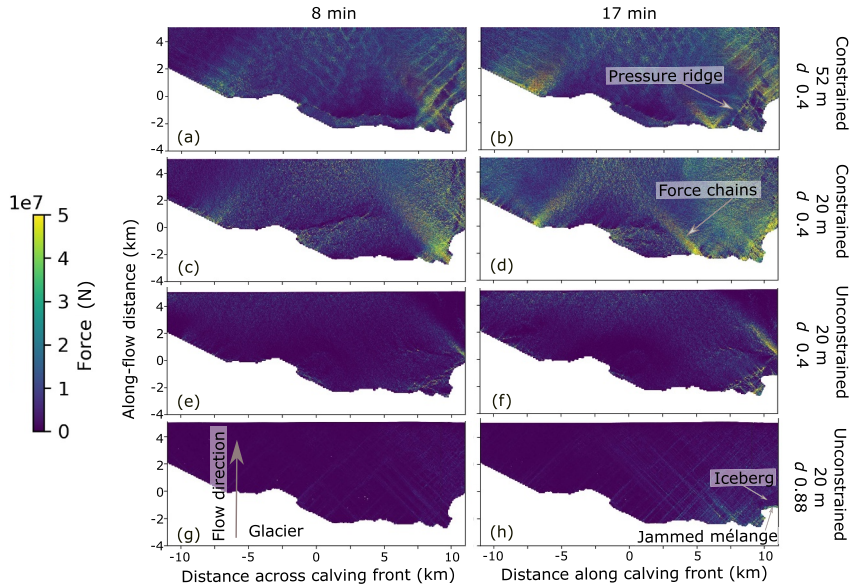

Figure 9. Compressive force between mélange particles over dynamic-time scales. The thickness of the synthetic mélange is noted as 20 or 52 m, *d* is the initial damage value assigned to the mélange, and 'unconstrained and "constrained" refer to limitations applied to mélange movement. The distance along the calving front corresponds to that shown in the 3D domain in Figure 2a.

aforementioned pressure ridges that built up in the mélange field of the simulation with a 52 m constrained mélange are apparent as well.

Force chains developed through the mélange field and remained intact over the duration of the constrained simulations. In the simulations with unconstrained mélange (Figures 9e–9h) there was greater disturbance within the initial mélange field and augmentation of compressive forces were minimal. A small zone of compression developed in the simulation with a strong unconstrained mélange due to disturbance in the mélange field (Figure 9f). Compression in the mélange in close proximity to the calving face in the eastern region of the domain is seen toward the end of both simulations with unconstrained mélange depicted in Figure 9 (panels f, h). This is a result of the forward displacement of the glacier with fracture growth and impending calving of a tabular iceberg (Figures 6a and 6b) or the build-up of mélange with the insertion of a small amount of newly calved debris. The latter is a transient event through which pressure builds and dissipates following calving events if the mélange is mobile. An example is seen in Figure 9h with mélange jammed directly behind a recently calved iceberg.

The backforce exerted on the calving face during two example simulations is shown with Hovmöller diagrams in Figure 10. The aforementioned increase in backforce in the eastern region of the weak, unconstrained simulation is seen in the left-hand panel of Figure 10. The backforce on the calving face remained low until approximately 26 hr of glacier sliding time when the calving event occurred on the glacier's promontory.

During the simulation with a constrained thick mélange, the backforce exerted on the calving face increased immediately following the initiation of the simulation. This constriction caused the backforce on the glacier to remain elevated across the calving face. The backforce was consistently elevated at the eastern edge of the domain, again at the location of the glacier promontory. In the western region of the domain, the development of force chains as the simulation progressed resulted in an increase in backforce on the calving front following approximately 14 hr of glacier sliding time. This is also seen in the east between approximately 6.5 and 10 km along the x axis. Strong force chains did not develop in the comparison simulation in which the weak mélange was unconstrained.

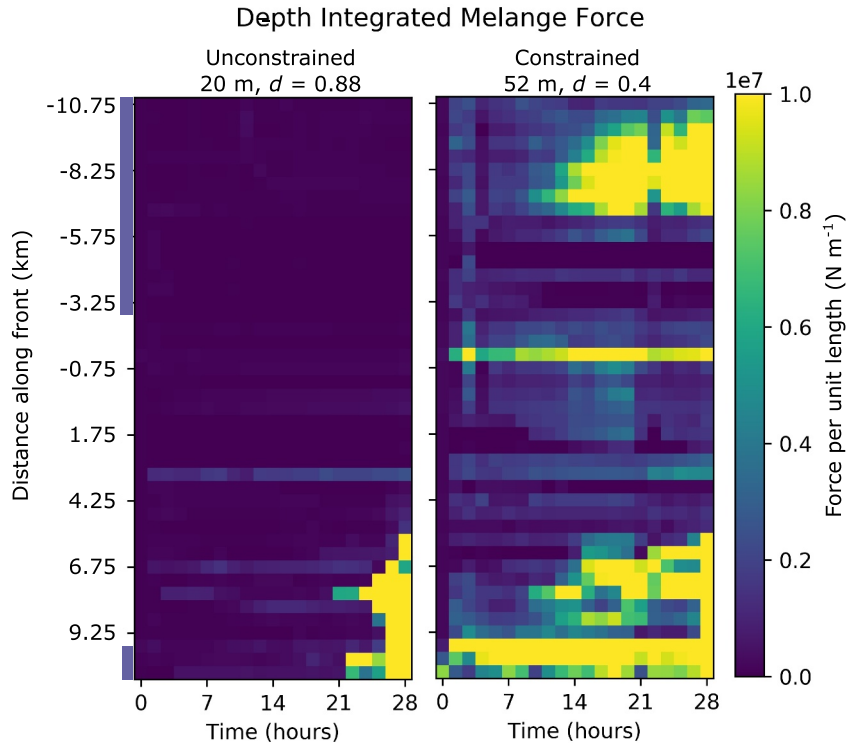

Figure 10. Depth-integrated backforce on the calving face over time for simulations in which the mélange is unconstrained, thin (20 m thickness) and weak ($d = 0.88$) (left) and constrained, thick (52 m thickness) and strong ($d = 0.4$) (right). The distance along the calving front corresponds to that shown in the 3D domain in Figure 2a. Blue-gray bars indicate positions of promontories across the glacier front.

4. Discussion

4.1. Ice Flow and Overhang Development

The Sentinel-1 imagery demonstrates the existence of a calving cycle in the WCF in which rifts form as ice is advected across the grounding line, followed by rift growth and calving (Movie S1; cf. Winberry et al., 2020). The HiDEM simulations in which ice push is applied exhibit longitudinal extension and calving close to the grounding line, and the production of tabular icebergs. We conclude that calving at the WCF occurs in response to a loss of basal traction and enhanced longitudinal strain as ice crosses the grounding line. The position of the calving front is therefore determined by the location of this region of enhanced strain near the grounding line. An important corollary of this is that the calving rate is simply the rate at which ice is delivered to the locus of enhanced strain and is equal (but opposite in sign) to the ice velocity. The significance of this can be appreciated by considering the consequence of an increase in velocity if other factors remained constant: the mean location of the calving front would remain near the point where basal traction is lost, but the calving rate would increase to match the ice flux. The calving rate, therefore, is an emergent property that depends upon factors that determine the calving location (ice thickness, basal topography, strain rate) and the ice velocity. This shows that calving laws based on predicting the position of the calving front (e.g., crevasse-depth calving laws: Benn et al., 2007; Nick et al., 2010; Todd et al., 2018) are more appropriate for predicting future evolution of WCF than calving laws that attempt to predict calving rates directly (e.g., Wilner et al., 2023).

Ice flow across the grounding line will likely continue to dominate the calving dynamics of the WCF as Thwaites Glacier evolves. In simulations of the evolution of Thwaites Glacier to 2100, DeConto et al. (2021) show that the fast-flowing core persists and expands over a wider region. The development of short, floating extensions will likely continue due to strain thinning and ocean-forced melting. The latter is currently an influential driver of thinning and corresponding grounding-line retreat for Thwaites Glacier (dos Santos et al., 2021). If retreat pushes the ice front into the over-deepening basin behind the bathymetric ridge on which it is currently grounded (Figure 1a), the calving face would increase in thickness, calve more readily and possibly be subject to ice-cliff

failure if cliff height and other glaciological conditions are met (Bassis et al., 2021; Crawford et al., 2021; DeConto et al., 2021).

There is a pronounced west to east increase in ice velocity across the WCF, resulting in shear strain across the domain. This is apparent in Figure 5b, as zones of elevated cumulative strain in the eastern part of the domain. At present, however, this shear strain does not appear to influence calving, which is instead associated with fresh fractures developed close to the grounding line. We note, however, that between 1995 and 2015, the fast-flowing core of Thwaites Glacier accelerated and extended westward (dos Santos et al., 2021) into our domain. If additional acceleration occurs, it is possible that shearing may play some role in calving dynamics at this location.

4.2. The Potential for Mélange to Influence Calving at the Thwaites Glacier WCF

Our results demonstrate the interplay between glacier flow, calving and the backforce applied to a glacier calving face. Sentinel-1 observations show an unconstrained mélange field that is fused by sea ice currently interacting with the WCF of Thwaites Glacier (Movie S1). In the HiDEM simulations of the WCF, glacier flow initially induces pressure within the mélange in a manner similar to that described by Amundson et al. (2010) and fittingly compared by Amundson and Burton (2018) to a bulldozer pushing forward a gravel pile. Our simulations show that the more efficient the bulldozer is in pushing the gravel pile forward (e.g., in simulations with a weak, unconstrained mélange), the more particles build up in front of it and then interact with the glacier calving face. When constrained, the mélange is compacted due to the forward advance of the terminus (Amundson et al., 2010), and when in such a jammed state (Cassotto et al., 2021), pressure appears in the form of force chains (Peters et al., 2015) that develop relatively long-lived resistance to calving and further forward flow of the glacier. Force chains stemming from resistive fjord sidewalls have previously been reported to inhibit the flow of a mélange field (Burton et al., 2018), though again the geometry of the ASE makes such lateral anchor points largely impossible. In our simulations, pressure from the flowing glacier continues to build up in a constrained mélange, causing buckling and shear that leads to pressure ridging.

When mélange is unconstrained in the presented simulations, forward flow of the glacier also builds up pressure within the mélange. Calving and fracture development can first occur given the relative freedom of movement compared with the simulations with a constrained mélange, supporting the statement by Cassotto et al. (2021) that the mechanical force available to the calving front is reduced in this unjammed mélange state. Local zones of compression are seen following calving events and this activity contributes to the build-up of backstress throughout the presented simulations, especially when the mélange is thick and loose. Local mélange compression and relaxation was described by Peters et al. (2015). The speed at which the transient force chains relax depends on the thickness and size-distribution within the mélange, the degree to which the mélange is constrained, and the degree to which the mélange is disturbed by calving and the forward pushing from the glacier. The slower the force chains relax, the more they can influence glacier calving. Looking further out from the duration of our simulations, we anticipate that how quickly the mélange can evacuate after the build-up of compressive stresses will be a key component governing further calving. As the simulations that included a mélange field were designed to simply test the importance of mélange containment on the calving dynamics across the Thwaites Glacier WCF, this study's set of simulations did not incorporate ocean and atmospheric drivers of mélange motion. Future studies may look to represent these driving forces in an assessment of the likelihood of mélange containment in this region of the ASE. Further, longer-duration simulations can also provide insight into the evolution of the glacier-mélange interactions as calving progresses and mélange evacuates (or not) from the embayment.

The flow of mélange (Figure 3) ahead of the WCF currently occurs in a manner that is more similar to the HiDEM simulations with an unconstrained mélange. Our HiDEM simulations highlight that, if constrained, mélange could substantially influence the calving dynamics of a domain representing the current configuration of the Thwaites Glacier terminus. As noted by Schlemm et al. (2022), the backforce provided by mélange will be influential on the future calving dynamics of Thwaites Glacier and Crawford et al. (2021) highlight that mélange buttressing is the rate-limiting factor for ice-cliff failure. Detailing one approach to represent mélange buttressing in ice-sheet modeling, Schlemm and Levermann (2021) contribute a parsimonious parameterization that considers embayment geometry, mélange properties, and mélange exit velocity from a fjord. In alignment with our simulation results, calving is reduced when mélange is constrained (i.e., has a low exit velocity). However, mélange will not be constrained laterally in the wide ASE in which Thwaites Glacier terminates. This differs from the situation of

tidewater glaciers that terminate in relatively narrow fjords, namely in Greenland, where mélange has been found previously to modulate calving dynamics (Bevan et al., 2019; Cassotto et al., 2015; Medrzycka et al., 2019; Moon et al., 2015; Xie et al., 2019).

Therefore, to provide enough backforce to inhibit calving, and particularly ice-cliff failure, mélange will need to be constrained by jamming behind a large grounded iceberg or by building up against the sea floor. Figure 4 shows an example of the movement of the mélange field being blocked by a small bathymetric high point. However, this type of blockage will need to occur across a greater spatial area to transmit enough pressure to the calving front to influence calving, which will be challenged by a greater driving force as retreat leads to deeper ice fronts (Cassotto et al., 2015). Further simulations of a synthetic geometry may also provide valuable insight into the relationship between mélange backforce and the size of grounded icebergs, as well as their location relative to a glacier terminating in a wide embayment. Additional modeling studies are needed to assess if mélange generated through future calving of the Thwaites Glacier will have sufficient keel depths to interact with bathymetric high points, such as the feature described as a past Thwaites Glacier grounding zone by Graham et al. (2022), and constrain the mélange in this vicinity.

4.3. The Role of Sea Ice

Our HiDEM simulations incorporated a synthetic mélange layer composed of particles representing small icebergs partly frozen together. This mélange was augmented during simulations by debris and calved icebergs. We suspect that the presence of sea ice, and specifically land-fast sea ice that hinders mélange movement as seen in the constrained-mélange simulations, will be influential in the future calving dynamics of the WCF. Seasonal sea-ice cycles have previously been shown to be closely linked to glacier retreat and advance (Carr et al., 2013), and it has been found that sea ice enhances the resistance mélange imparted on a glacier's calving face by increasing the critical shear strength of the mélange field (Amundson et al., 2010). Land-fast sea ice also currently holds together the extensively fragmented TT (Miles et al., 2020).

Though Cassotto et al. (2021) demonstrated that mélange can influence glacier calving in the absence of this binding sea ice, land-fast sea ice will very likely be a necessary "glue" across the iceberg-debris field to allow for the transmission of pressure across the wide embayment to the Thwaites Glacier terminus, with thicker sea ice transmitting greater resistive forces to the calving face (Robel, 2017).

The rigidity of the mélange, largely influenced by the characteristics of binding sea ice, will be an influential factor in the degree to which calving can be suppressed (Joughin et al., 2020; Robel, 2017). Grounded icebergs may also aid in the anchoring of the landfast sea ice, as has been the case for iceberg B-22 in the ASE (Miles et al., 2020). These interactions highlight the need to overcome challenges (Amundson & Burton, 2018) to represent mélange fields in tidewater-glacier models (Cassotto et al., 2021) and ice-sheet models, with the additional requirement to couple the sea-ice and ice-sheet components of Earth system models.

5. Conclusions

We applied a new version of HiDEM to unravel the factors that contribute to the current calving dynamics at the WCF of Thwaites Glacier, as well as to investigate the potential influence of mélange on calving at this location. Growth of short ice-shelf extensions and the loss of basal traction as ice crosses the grounding line were found to play a dominant role in the current calving dynamics at the WCF. These factors are expected to continue influencing calving dynamics as Thwaites Glacier evolves. We expect that the ability for mélange to put the brakes on calving will be a substantial factor in the future calving dynamics and retreat of Thwaites Glacier, especially as calving could become a more dominant retreat mechanism given the deeper calving fronts that could be exposed if the grounding line retreats from the bathymetric ridge on which it currently resides.

Our simulations demonstrate that mélange must be highly constrained to impede the calving dynamics at the WCF in its current configuration. This allows for force chains that have previously been found to influence calving in narrow fjords in Greenland to form, transmit force and modify calving dynamics in wide embayments, *if* a blockage of suitable size exists (e.g., a large, grounded iceberg). The containment of mélange within the sector of the wide ASE into which the Thwaites Glacier terminates will be influenced by the presence and characteristics of sea ice as well as the morphology of the mélange itself. An important next step to determine the fate of Thwaites Glacier includes modeling of the size distribution of future icebergs calved from evolved calving fronts to

determine if iceberg keels will be sufficiently deep to interact with seafloor features. Our findings also support the need to integrate sea ice, mélange and glacier/ice-sheet processes into a single modeling framework, no small feat but one that is required to constrain projections of SLR contributions from the Antarctic Ice Sheet.

Data Availability Statement

All data utilized in this study are available through online repositories. Sentinel-1 SAR data are available through the Copernicus Open Data Hub (https://browser.dataspace.copernicus.eu). For this study, Sentinel-1 'Interferometric Wide—IW' images were selected covering the area of interest at geographic coordinate −107°W, −75°S. BedMachine v2 (Morlighem, 2020), which was used to build the 3D model domain, is available at https://doi.org/10.5067/E1QL9HFQ7A8M. Thwaites Glacier velocity data, used in the inversion for basal resistance, was obtained from the MEaSUREs project and is available at https://nsidc.org/data/nsidc-0484/versions/2 (Rignot et al., 2017). Elmer/Ice is an open/access glacier model that is available at https://doi.org/10.5281/zenodo.7892181 (Ruokolainen et al., 2023). The Helsinki Discrete Element Model is available at https://doi.org/10.5281/zenodo.7849148 (van Dongen & Todd, 2023).

Acknowledgments
We greatly appreciate the time that three anonymous reviewers and the journal editor dedicated to assessing the presented research. This work used the ARCHER2 UK National Supercomputing Service (https://www.archer2.ac.uk) and was conducted as part of the DOMINOS component of the International Thwaites Glacier Collaboration with support from the Natural Environment Research Council (NERC: Grant NE/S006605/1). Logistics provided by NSF-U.S. Antarctic Program and NERC-British Antarctic Survey. ITGC Contribution No. ITGC-082. The authors also wish to acknowledge the CSC-IT Center for Science, Finland, for computational resources. Computations on CSC's platforms were supported by the HPC-Europa3 program, part of the European Union's Horizon 2020 research and innovation programme under grant agreement No.730897. TanDEM-X data used for generating the DEMs and floatation heights were supplied by DLR. Rupert Gladstone and Thomas Zwinger are supported by the Academy of Finland project COLD under consortium Grants 322430 and 322978. AC was supported by the Leverhulme Trust as an Early Career Fellow (Grant 2021-440).

References

Alley, K. E., Wild, C. T., Luckman, A., Scambos, T. A., Truffer, M., Pettit, E. C., et al. (2021). Two decades of dynamic change and progressive destabilization on the Thwaites Eastern Ice Shelf. *The Cryosphere*, *15*(11), 5187–5203. https://doi.org/10.5194/tc-2021-76

Amundson, J. M., & Burton, J. C. (2018). Quasi-static granular flow of ice mélange. *Journal of Geophysical Research: Earth Surface*, *123*(9), 2243–2257. https://doi.org/10.1029/2018JF004685

Amundson, J. M., Fahnestock, M., Truffer, M., Brown, J., Lüthi, M. P., & Motyka, R. J. (2010). Ice mélange dynamics and implications for terminus stability, Jakobshavn Isbræ, Greenland. *Journal of Geophysical Research*, *115*(F1). https://doi.org/10.1029/2009JF001405

Åström, J., Cook, S., Enderlin, E. M., Sutherland, D. A., Mazur, A., & Glasser, N. (2021). Fragmentation theory reveals processes controlling iceberg size distributions. *Journal of Glaciology*, *67*(264), 603–612. https://doi.org/10.1017/jog.2021.14

Åström, J. A., & Benn, D. I. (2019). Effective rheology across the fragmentation transition for sea ice and ice shelves. *Geophysical Research Letters*, *46*(22), 13099–13106. https://doi.org/10.1029/2019GL084896

Åström, J. A., Riikilä, T. I., Tallinen, T., Zwinger, T., Benn, D., Moore, J. C., & Timonen, J. (2013). A particle based simulation model for glacier dynamics. *The Cryosphere*, *7*(5), 1591–1602. https://doi.org/10.5194/tc-7-1591-2013

Åström, J. A., Vallot, D., Schäfer, M., Welty, E. Z., O'Neel, S., Bartholomaus, T. C., et al. (2014). Termini of calving glaciers as self-organized critical systems. *Nature Geoscience*, *7*(12), 874–878. https://doi.org/10.1038/ngeo2290

Bassis, J. N., Berg, B., Crawford, A. J., & Benn, D. I. (2021). Transition to marine ice cliff instability controlled by ice thickness gradients and velocity. *Science*, *372*(6548), 1342–1344. https://doi.org/10.1126/science.abf6271

Benn, D. I., Åström, J., Zwinger, T., Todd, J., Nick, F. M., Cook, S., et al. (2017). Melt-under-cutting and buoyancy-driven calving from tidewater glaciers: New insights from discrete element and continuum model simulations. *Journal of Glaciology*, *63*(240), 691–702. https://doi.org/10.1017/jog.2017.41

Benn, D. I., Hulton, N. R., & Mottram, R. H. (2007). Calving laws', 'sliding laws' and the stability of tidewater glaciers. *Annals of Glaciology*, *46*, 123–130. https://doi.org/10.3189/172756407782871161

Benn, D. I., Luckman, A., Åström, J. A., Crawford, A. J., Cornford, S. L., Bevan, S. L., et al. (2022). Rapid fragmentation of Thwaites Eastern Ice Shelf. *The Cryosphere*, *16*(6), 2545–2564. https://doi.org/10.5194/tc-16-2545-2022

Bevan, S. L., Luckman, A. J., Benn, D. I., Adusumilli, S., & Crawford, A. (2021). Brief communication: Thwaites Glacier cavity evolution. *The Cryosphere*, *15*(7), 3317–3328. https://doi.org/10.5194/tc-15-3317-2021

Bevan, S. L., Luckman, A. J., Benn, D. I., Cowton, T., & Todd, J. (2019). Impact of warming shelf waters on ice mélange and terminus retreat at a large SE Greenland glacier. *The Cryosphere*, *13*(9), 2303–2315. https://doi.org/10.5194/tc-13-2303-2019

Burton, J. C., Amundson, J. M., Cassotto, R., Kuo, C.-C., & Dennin, M. (2018). Quantifying flow and stress in ice mélange, the world's largest granular material. *Proceedings of the National Academy of Sciences of the United States of America*, *115*(20), 5105–5110. https://doi.org/10.1073/pnas.1715136115

Carr, J. R., Vieli, A., & Stokes, C. (2013). Influence of sea ice decline, atmospheric warming, and glacier width on marine-terminating outlet glacier behavior in northwest Greenland at seasonal to interannual timescales. *Journal of Geophysical Research: Earth Surface*, *118*(3), 1210–1226. https://doi.org/10.1002/jgrf.20088

Cassotto, R., Fahnestock, M., Amundson, J. M., Truffer, M., & Joughin, I. (2015). Seasonal and interannual variations in ice mélange and its impact on terminus stability, Jakobshavn Isbræ, Greenland. *Journal of Glaciology*, *61*(225), 76–88. https://doi.org/10.3189/2015JoG13J235

Cassotto, R. K., Burton, J. C., Amundson, J. M., Fahnestock, M. A., & Truffer, M. (2021). Granular decoherence precedes ice mélange failure and glacier calving at Jakobshavn Isbræ. *Nature Geoscience*, *14*(6), 417–422. https://doi.org/10.1038/s41561-021-00754-9

Christie, F. D. W., Benham, T. J., Batchelor, C. L., Rack, W., Montelli, A., & Dowdeswell, J. A. (2022). Antarctic ice-shelf advance driven by anomalous atmospheric and sea-ice circulation. *Nature Geoscience*, *15*(5), 356–362. https://doi.org/10.1038/s41561-022-00938-x

Cook, S., Åström, J., Zwinger, T., Galton-Fenzi, B. K., Greenbaum, J. S., & Coleman, R. (2018). Modelled fracture and calving on the Totten Ice Shelf. *The Cryosphere*, *12*(7), 2401–2411. https://doi.org/10.5194/tc-12-2401-2018

Copernicus Open Data Hub. (n.d.). Copernicus Sentinel-1 data. [Dataset]. *ESA*. Retrieved from https://scihub.copernicus.eu/

Crawford, A. J., Benn, D. I., Todd, J., Åström, J. A., Bassis, J. N., & Zwinger, T. (2021). Marine ice-cliff instability modeling shows mixed-mode ice-cliff failure and yields calving rate parameterization. *Nature Communications*, *12*(1), 2701. https://doi.org/10.1038/s41467-021-23070-7

DeConto, R. M., & Pollard, D. (2016). Contribution of Antarctica to past and future sea-level rise. *Nature*, *531*(7596), 591–597. https://doi.org/10.1038/nature17145

DeConto, R. M., Pollard, D., Alley, R. B., Velicogna, I., Gasson, E., Gomez, N., et al. (2021). The Paris Climate Agreement and future sea-level rise from Antarctica. *Nature*, *593*(7857), 83–89. https://doi.org/10.1038/s41586-021-03427-0

dos Santos, T. D., Barnes, J. M., Goldberg, D. N., Gudmundsson, G. H., & Morlighem, M. (2021). Drivers of change of Thwaites Glacier, west Antarctica, between 1995 and 2015. *Geophysical Research Letters*, *48*(20), e2021GL093102. https://doi.org/10.1029/2021GL093102
Gagliardini, O., Zwinger, T., Gillet-Chaulet, F., Durand, G., Favier, L., de Fleurian, B., et al. (2013). Capabilities and performance of Elmer/Ice, a new-generation ice sheet model. *Geoscientific Model Development*, *6*(4), 1299–1318. https://doi.org/10.5194/gmd-6-1299-2013
Gladstone, R., & Wang, Y. (2022). *Antarctic regional inversions using Elmer/Ice: Methodology*. Zenodo. https://doi.org/10.5281/zenodo.5862046
Graham, A. G. C., Wåhlin, A., Hogan, K. A., Nitsche, F. O., Heywood, K. J., Totten, R. L., et al. (2022). Rapid retreat of Thwaites Glacier in the pre-satellite era. *Nature Geoscience*, *15*(9), 706–713. https://doi.org/10.1038/s41561-022-01019-9
Joughin, I., Shean, D. E., Smith, B. E., & Floricioiu, D. (2020). A decade of variability on Jakobshavn Isbræ: Ocean temperatures pace speed through influence on mélange rigidity. *The Cryosphere*, *14*(1), 211–227. https://doi.org/10.5194/tc-14-211-2020
Khazendar, A., Rignot, E., & Larour, E. (2009). Roles of marine ice, rheology, and fracture in the flow and stability of the Brunt/Stancomb-Wills Ice Shelf. *Journal of Geophysical Research*, *114*(F4), F04007. https://doi.org/10.1029/2008JF001124
Lhermitte, S., Sun, S., Shuman, C., Wouters, B., Pattyn, F., Wuite, J., et al. (2020). Damage accelerates ice shelf instability and mass loss in Amundsen Sea Embayment. *Proceedings of the National Academy of Sciences of the United States of America*, *117*(40), 201912890–201924741. https://doi.org/10.1073/pnas.1912890117
Luckman, A., Benn, D. I., Cottier, F., Bevan, S., Nilsen, F., & Inall, M. (2015). Calving rates at tidewater glaciers vary strongly with ocean temperature. *Nature Communications*, *6*(1), 8566. https://doi.org/10.1038/ncomms9566
Medrzycka, D., Copland, L., Van Wychen, W., & Burgess, D. (2019). Seven decades of uninterrupted advance of Good Friday Glacier, Axel Heiberg Island, Arctic Canada. *Journal of Glaciology*, *65*(251), 440–452. https://doi.org/10.1017/jog.2019.21
Miles, B. W. J., Stokes, C. R., Jenkins, A., Jordan, J. R., Jamieson, S. S. R., & Gudmundsson, G. H. (2020). Intermittent structural weakening and acceleration of the Thwaites Glacier Tongue between 2000 and 2018. *Journal of Glaciology*, *66*(257), 1–11. https://doi.org/10.1017/jog.2020.20
Moon, T., Joughin, I., & Smith, B. (2015). Seasonal to multiyear variability of glacier surface velocity, terminus position, and sea ice/ice mélange in northwest Greenland. *Journal of Geophysical Research: Earth Surface*, *120*(5), 818–833. https://doi.org/10.1002/2015JF003494
Morlighem, M. (2020). MEaSUREs BedMachine Antarctica, version 2 [Dataset]. *NASA National Snow and Ice Data Center Distributed Active Archive Center*. https://doi.org/10.5067/E1QL9HFQ7A8M
Morlighem, M., Rignot, E., Binder, T., Blankenship, D., Drews, R., Eagles, G., et al. (2020). Deep glacial troughs and stabilizing ridges unveiled beneath the margins of the Antarctic ice sheet. *Nature Geoscience*, *13*(2), 132–137. https://doi.org/10.1038/s41561-019-0510-8
Mouginot, J., Rignot, E., & Scheuchl, B. (2014). Sustained increase in ice discharge from the Amundsen Sea Embayment, West Antarctica, from 1973 to 2013. *Geophysical Research Letters*, *41*(5), 1576–1584. https://doi.org/10.1002/2013GL059069
Nick, F. M., Van der Veen, C. J., Vieli, A., & Benn, D. I. (2010). A physically based calving model applied to marine outlet glaciers and implications for the glacier dynamics. *Journal of Glaciology*, *56*(199), 781–794. https://doi.org/10.3189/002214310794457344
Otero, J., Navarro, F. J., Lapazaran, J. J., Welty, E., Puczko, D., & Finkelnburg, R. (2017). Modeling the controls on the front position of a Tidewater Glacier in Svalbard. *Frontiers in Earth Science*, *5*. https://doi.org/10.3389/feart.2017.00029
Peters, I. R., Amundson, J. M., Cassotto, R., Fahnestock, M., Darnell, K. N., Truffer, M., & Zhang, W. W. (2015). Dynamic jamming of iceberg-choked fjords. *Geophysical Research Letters*, *42*(4), 1122–1129. https://doi.org/10.1002/2014GL062715
Rignot, E., Mouginot, J., & Scheuchl (2017). MEaSUREs InSAR-based Antarctica ice velocity map, version 2 [Dataset]. *NASA National Snow and Ice Data Center DAAC*. https://doi.org/10.5067/D7GK8F5J8M8R
Rignot, E., Mouginot, J., & Scheuchl, B. (2016). *MEaSUREs Antarctic grounding line from differential satellite radar interferometry, version 2*. NASA DAAC at the National Snow and Ice Data Center Distributed Active Archive Center. https://doi.org/10.5067/IKBWW4RYHF1Q
Rignot, E., Mouginot, J., Scheuchl, B., van den Broeke, M., van Wessem, M. J., & Morlighem, M. (2019). Four decades of Antarctic Ice Sheet mass balance from 1979–2017. *Proceedings of the National Academy of Sciences of the United States of America*, *116*(4), 1095–1103. https://doi.org/10.1073/pnas.1812883116
Robel, A. A. (2017). Thinning sea ice weakens buttressing force of iceberg mélange and promotes calving. *Nature Communications*, *8*(1), 14596. https://doi.org/10.1038/ncomms14596
Ruokolainen, J., Malinen, M., Råback, P., Zwinger, T., Takala, E., Kataja, J., et al. (2023). ElmerCSC/elmerfem: Elmer 9.0 (release-9.0) [software]. *Zenodo*. https://doi.org/10.5281/zenodo.7892181
Scambos, T. A., Bell, R. E., Alley, R. B., Anandakrishnan, S., Bromwich, D. H., Brunt, K., et al. (2017). How much, how fast? A science review and outlook for research on the instability of Antarctica's Thwaites Glacier in the 21st century. *Global and Planetary Change*, *153*, 16–34. https://doi.org/10.1016/j.gloplacha.2017.04.008
Schlemm, T., Feldmann, J., Winkelmann, R., & Levermann, A. (2022). Stabilizing effect of mélange buttressing on the Marine Ice Cliff Instability of the West Antarctic Ice Sheet. *The Cryosphere*, *16*. https://doi.org/10.5194/tc-2021-238
Schlemm, T., & Levermann, A. (2021). A simple parametrization of mélange buttressing for calving glaciers. *The Cryosphere*, *15*(2), 531–545. https://doi.org/10.5194/tc-15-531-2021
Sergienko, O., & Haseloff, M. (2023). 'Stable' and 'unstable' are not useful descriptions of marine ice sheets in the Earth's climate system. *Journal of Glaciology*, *69*(277), 1483–1499. https://doi.org/10.1017/jog.2023.40
Sergienko, O. V. (2022). Marine outlet glacier dynamics, steady states and steady-state stability. *Journal of Glaciology*, 1–15. https://doi.org/10.1017/jog.2022.13
Sergienko, O. V., & Wingham, D. J. (2022). Bed topography and marine ice-sheet stability. *Journal of Glaciology*, *68*(267), 124–138. https://doi.org/10.1017/jog.2021.79
Todd, J., Christoffersen, P., Zwinger, T., Råback, P., Chauché, N., Benn, D., et al. (2018). A full-Stokes 3-D calving model applied to a large Greenlandic glacier. *Journal of Geophysical Research: Earth Surface*, *123*(3), 410–432. https://doi.org/10.1002/2017jf004349
Vallot, D., Åström, J., Zwinger, T., Pettersson, R., Everett, A., Benn, D. I., et al. (2018). Effects of undercutting and sliding on calving: A global approach applied to Kronebreen, Svalbard. *The Cryosphere*, *12*(2), 609–625. https://doi.org/10.5194/tc-12-609-2018
van Dongen, E. C. H., Åström, J. A., Jouvet, G., Todd, J., Benn, D. I., & Funk, M. (2020). Numerical modeling shows increased fracturing due to melt-undercutting prior to major calving at Bowdoin Glacier. *Frontiers in Earth Science*, *8*. https://doi.org/10.3389/feart.2020.00253
van Dongen, E. C. H., & Todd, J. (2023). joeatodd/HiDEM: Performance improvements & bug fixes (v2.1.1) [software]. *Zenodo*. https://doi.org/10.5281/zenodo.7849148
Wang, Y., Zhao, C., Gladstone, R., Galton-Fenzi, B., & Warner, R. (2022). Thermal structure of the Amery Ice Shelf from borehole observations and simulations. *The Cryosphere*, *16*(4), 1221–1245. https://doi.org/10.5194/tc-16-1221-2022
Wild, C. T., Alley, K. E., Muto, A., Truffer, M., Scambos, T. A., & Pettit, E. C. (2022). Weakening of the pinning point buttressing Thwaites Glacier, West Antarctica. *The Cryosphere*, *16*, 397–417. https://doi.org/10.5194/tc-2021-130

Wilner, J. A., Morlighem, M., & Cheng, G. (2023). Evaluation of four calving laws for Antarctic ice shelves. *The Cryosphere*, *17*(11), 4889–4901. https://doi.org/10.5194/tc-17-4889-2023

Winberry, J. P., Huerta, A. D., Anandakrishnan, S., Aster, R. C., Nyblade, A. A., & Wiens, D. A. (2020). Glacial earthquakes and precursory seismicity associated with Thwaites Glacier calving. *Geophysical Research Letters*, *47*(3). https://doi.org/10.1029/2019GL086178

Xie, S., Dixon, T. H., Holland, D. M., Voytenko, D., & Vaňková, I. (2019). Rapid iceberg calving following removal of tightly packed pro-glacial mélange. *Nature Communications*, *10*(1), 3250. https://doi.org/10.1038/s41467-019-10908-4